Soft Matter

Viscous liquid-liquid wetting and dewetting of textured surfaces

Journal:	*Soft Matter*
Manuscript ID	SM-ART-08-2020-001524.R1
Article Type:	Paper
Date Submitted by the Author:	25-Oct-2020
Complete List of Authors:	Hu, Xiaoyi; Stony Brook University, Mechanical engineering Wang, Zhen; Stony Brook University, Mechanical engineering Hwang, David; Stony Brook University, Mechanical Engineering Colosqui, Carlos; Stony Brook University, Mechanical Engineering Cubaud, Thomas; Stony Brook University, Mechanical engineering

Viscous liquid-liquid wetting and dewetting of textured surfaces

Xiaoyi Hu, Zhen Wang, David J. Hwang, Carlos E. Colosqui and Thomas Cubaud*

Department of Mechanical Engineering, Stony Brook University, Stony Brook, NY, 11794, USA

Abstract

We experimentally investigate the spreading and receding behavior of small water droplets immersed in viscous oils on grid-patterned surfaces using synchronized bottom and profile views. In particular, the evolution of apparent advancing and receding contact angles of droplets fed at constant flow rate is studied as a function of grid surface coverage and height for a wide range of external phase viscosity. Detailed examination of droplet aspect ratio during inflation process provides an averaging method for characterization of quasi-static advancing angles on heterogeneous surfaces. Droplets spreading in partial Cassie state on planar microfluidic grids are also shown to capture oil patches that further evolve into trapped oil droplets depending on grid aspect ratio. The natural retraction velocity of thin water films is examined based on external phase velocity and regime maps of trapped droplets are delineated based on control parameters.

E-Mail: thomas.cubaud@stonybrook.edu

1. Introduction

Liquid-liquid wetting occurs in many natural and industrial processes, such as enhanced oil recovery,[1-3] oil-water separation,[4,5] and self-cleaning surfaces.[6,7] While the wetting characteristics of liquid-gas systems have been widely studied,[8-11] the presence of a viscous external phase is known to strongly influence wetting dynamics on plane and liquid-infused surfaces as well as in porous media.[12-17] Describing the wetting properties of two liquids in contact with a solid surface is particularly challenging due to the presence of two viscosity coefficients thereby limiting the use capillary numbers.[18] In addition, most surfaces of interests are rough and chemically heterogeneous and equilibrium contact angles present significant deviations from Young's equation.

Droplets deposited on rough surfaces in air are typically classified into two wetting states, including the Wenzel state,[19] where droplets wet the total surface area, and the Cassie state[20] in which droplets do not permeate the surface texture and only wet the top of surface asperities. Intermediate wetting states are also commonly observed and various models have been developed to predict droplet behavior on complex surfaces.[21-24] The chemical affinity, topography, and arrangement of decorated surfaces, such as disconnected arrays of micropillars, individual cavities or continuous grid patterns, have been found to play an important role on contact angles[25-30] and wetted area morphology, including during the formation of polygonal drops.[31-34] In general, a difficulty in defining contact angles on composite surface resides with the local variation of the contact angle along the contact line due to pinning sites and complex stick-and-slip motion can lead to the trapping of air bubbles during fast leaping motions.[35] In addition to local topography, contact angles also depend on contact line velocity and display large hysteresis between advancing and receding motion.[36,37] In the context of liquid-liquid wetting, liquid-infused surfaces present significant advantage for manipulating contact angles.[38-41] Less is known, however, about the spreading and receding behavior of immersed droplets fed at constant flow rate on decorated surfaces.

In this work, we examine the wetting dynamics of water droplets surrounded in viscous oils on grid-textured surfaces. We show that grating provides strong pinning sites to manipulate water droplet shape and contact angle, and grid cavities form arrays of dead-end pores that capture minute oil droplets. The aspect ratio of water droplets fed and withdrawn at constant flow rate is first investigated. Recently, we developed a method for measuring quasi-static advancing contact angle of droplets fed at constant flow rate in air based on growth rate.[42] Here, we compare direct measurements of apparent contact angles of water droplets immersed in oil with a spherical cap model. The shape of the wetted area is characterized based on surface coverage to quantify the evolution of the radius of curvature of faceted droplets. During the withdrawal process, a thin water film is left and observed to spontaneously retract at longer times. We investigate the relationship between the characteristic film dewetting velocity and outer oil viscosity coefficients. Finally, we discuss the occurrence of trapped oil droplets during the slow water drop spreading process, leading to partial Cassie states. Regime maps are examined to characterize the oil trapping process based on pores aspect ratio and fluid properties. The extended period of time combined with high-resolution microscopy enables access to a wide range of natural and forced interfacial velocities.

2. Experimental methods

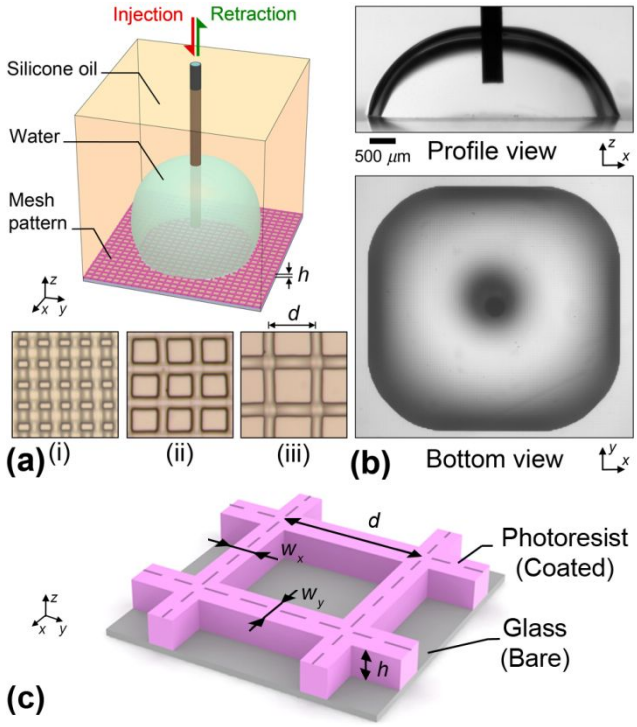

Fig. 1 Experimental apparatus. (a) Top: Schematics of setup for oil-immersed water droplet spreading and receding on textured surfaces. Bottom: Micrographs of laser-patterned microfluidic grids, (i) d = 15, (ii) d = 25, and (iii) 35 μm. (b) Synchronous profile and bottom views for characterization of free surface and wetted area evolution. Water in 10-cS oil on surface 1*b* with d = 30 μm. (c) Schematics of grid characteristics.

The experimental setup includes a patterned glass slide resting at the bottom surface of a rectangular transparent cell filled with silicone oil. A microneedle is mounted on a miniature XYZ stage and positioned above the substrate to first inject and then withdraw water using a syringe pump operating at volumetric flow rate Q [Fig. 1(a)]. Synchronous orthogonal views of the process are captured with high-resolution cameras equipped with a telemetric zoom for the profile view and an extension tube for the bottom view [Fig. 1(b)]. Patterns consist of square grids with a mesh size d = 15, 20, 25, 30, 35, 40, 55 and 85 μm and height h_1 = 5 or h_2 = 9 μm. A two-photon polymerization technique is used with a picosecond laser to pattern photoresist (NOA61 resin) using standard microfabrication techniques.[43,44] Taking into account the widths of the grids w_x = 7.6 and w_y = 10.1 μm resulting from the laser scanning process, the grid surface coverage is defined as $\sigma = 1 - (d - w_x)(d - w_y)/d^2$, where $\sigma = 0$ corresponds to the glass substrate and $\sigma = 1$ is associated with a fully coated surface. Conversely, the surface coverage of cavities delineated by the grid patterning corresponds to $1 - \sigma$ [Fig. 1(c)].

To examine the influence of surface composition, two types of substrates are tested, including those where grids are built on the bare glass, which are referred to as 'bare', and those where meshes are built on a coated layer of the same photoresist, which are referred to as 'coated'. Two heights, h_1 and h_2, are tested for each type of coating. Hence, substrates are labelled according to grid height and coating condition. For instance, a substrate with a mesh of height of $h = 9$ μm built on a bare surface is referred to as surface 2*b*.

As previous work has shown the predominance of the outer phase viscosity η_2 over the inner phase viscosity η_1 during the initial spreading of immersed droplets on smooth surfaces,[18] experiments are conducted with drops made of DI water, having viscosity $\eta_1 = 1$ cP, in an outer phase made of silicone oils of various viscosities, such as $\eta_2 = 9.3$, 97, and 971 cP using surfaces 1*b* at various *d*. These oils are usually referred in the text based on their kinematic viscosities of 10^1, 10^2, and 10^3 cS respectively, for simplicity. In general, all surfaces are tested using a single fluid pair made of DI water and 100-cS oil. This fluid pair is used as a standard reference unless otherwise specified in the text.

The interfacial tension γ_{12} between the water and oils investigated in this work remains constant $\gamma_{12} \approx 42.7$ mN/m. As viscous silicone fluids correspond to heavy oils, the density difference $\Delta\rho = \rho_1 - \rho_2$ with water is small, which leads to relatively large capillary lengths $\lambda_C = [\gamma_{12}/(\Delta\rho g)]^{1/2} \sim 10$ mm. Hence, droplets with height $H \sim 1$ mm have small Bond numbers $Bo = (H/\lambda_C)^2 \sim 10^{-2}$ and the shape of the free surface between water and oil is expected to adopt a minimal surface area configuration, including spherical cap morphologies due to the absence of significant gravitational effects during quasi-static deformation.

Therefore, our apparatus enables access to a form of reduced gravity environment where contact angles can be inferred from analysis of free surface shape during the slow deformation of sessile drops. This method allows for an average measurement of contact angles on chemically different surfaces, which are compared to local apparent contact angles observed during spreading on rough surfaces.

3. Inflation and deflation of immersed drops

We first examine the morphology and dynamics of immersed droplet spreading and receding from composite surfaces as illustrated on Fig. 2(a). Parameters of interests comprise the base diameter of the wetted area *D*, the droplet height *H* from the substrate, and the apparent contact angle θ obtained from the profile view. It is instructive to examine the evolution of the droplet aspect ratio $\Gamma = H/D$, which is shown to monotonically decrease during the entire injection-retraction process [Fig. 2(b)]. Two main stages are based on the set flow rate $Q = 2$ μL/min used for infusion and retraction. The inflation stage takes place at constant *Q* and consists of two phases, including (i) initial pendant drop contact at early times and (ii) sustained growth between t_1 and t_2. The flow rate is turned off at instant t_2 to allow for (iii) the natural droplet relaxation. While some droplets tend to growth asymmetrically from the injection needle, the evolution of wetted area remains consistent for a parametric study

and the needle is repositioned in the center of the droplet before inverting Q at t_3 to ensure a symmetrical deflation process. The deflation stage is separated into three phases with (iv) a withdrawal period where most of the droplet volume is decreased with fixed contact line, followed by (v) an apparent dewetting stage starting at t_4 where the receding liquid wedge is extracted leaving a thin water film at the surface. At the end of the apparent dewetting stage, a small droplet is usually left on the surface near the suction location. The flow rate is turned off at t_5 to allow for observing (vi) the natural film retraction on surfaces of various topologies. The contact line velocity $V = dD/(2dt)$ significantly decreases during the inflation stage, ranging from $V \sim 10^{-2}$ m/s when the immersed drop makes initial contact with the surface[18] to a few microns per second during the sustained growth period and $V \sim 10^{-7}$ m/s in the relaxation phase,[16] which corresponds to very low capillary numbers $\mathrm{Ca}_1 = \eta_1 V/\gamma_{12} \sim 10^{-7}$ [Fig. 2(c)].

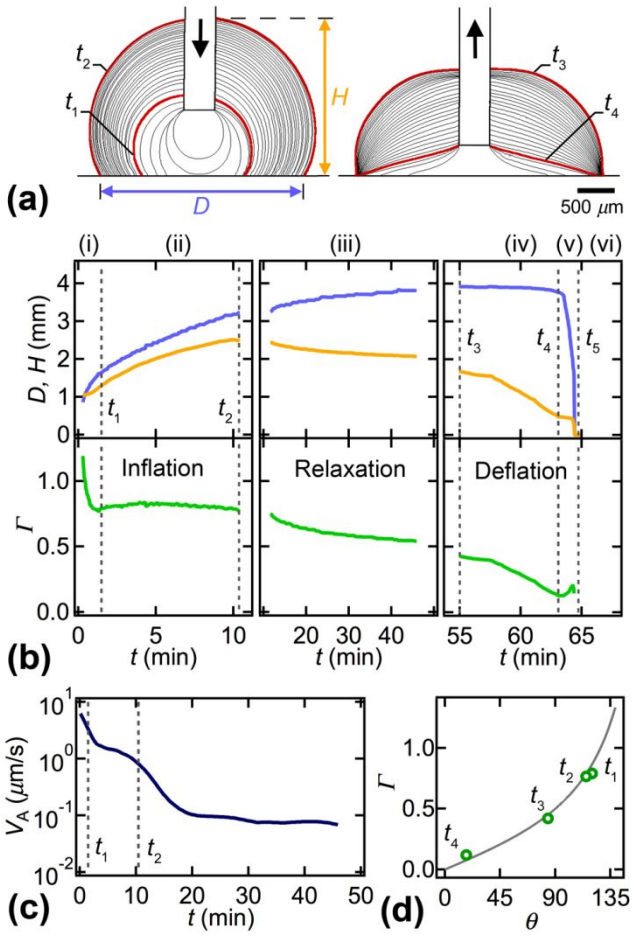

Fig. 2 Growth and withdrawal of a sessile drop in a viscous phase. (a) Superimposed time-series of growth (left) and withdrawal (right) stages of a water droplet in 100 cS-oil on surface 1*b* with $d = 30$ μm, $\Delta t = 20$ s. Thick red lines correspond to stage transitions. (b) Temporal evolution of base diameter D, droplet height H, and aspect ratio Γ during inflation and deflation processes: (i) initial spreading, (ii) sustained growth, (iii) relaxation, (iv) withdrawal, (v) apparent dewetting, and

(vi) film retraction. (c) Smoothed contact line velocity as a function of time during sustained growth and relaxation stages. (d) Relationship between Γ and measured contact angle θ at stage transitions. Solid line: Eq. 1.

Using a quasi-static assumption, the free surface is expected to conform to a spherical shape to minimize interfacial area. In the case of smooth surfaces, the relationship between the height-to-base diameter ratio $\Gamma = H/D$ and contact angle θ for a spherical cap is based on geometry according to

$$\frac{H}{D} = \frac{1-\cos\theta}{2\sin\theta} \quad \text{Eq. 1}$$

In figure 2(d), we compare independent measurements of Γ and θ from the profile views with Eq. 1 across the various stages and find relatively good agreement between model and experiment. Therefore, the droplet aspect ratio Γ provides a useful parameter to characterize small immersed droplets contact angles on heterogeneous surfaces. By contrast, for large sessile drops flattened by gravity in ambient air, the average contact angle θ on a composite surface can be determined form the height H only.[28] Here, during the sustained growth period, the aspect Γ is found to remain constant [Fig. 2(b)], which provides complementary information for characterizing advancing contact angle on textured surfaces.

4. Apparent advancing contact angles

Surface patterning strongly affect dynamic contact angles. As the surface coverage σ ranges between two smooth surfaces for $\sigma = 0$ and 1, with respective advancing contact angles $\theta_{AB} = 55$ on the bare surface and $\theta_{AC} = 78 \pm 3$ degrees on the coated surface, the maximum apparent advancing contact angle θ_{A0} measured during sustained growth on textured surfaces shows significant increase to about 120 degrees for intermediate value of σ [Fig. 3(a)]. Such large values of θ_{A0} suggest strong contact line pinning[11] at the edge of grid lines having characteristic angle $\phi = \pi/2$ with the possibility of a maximum, local apparent contact angle $\theta_{AM} = \pi - \phi + \theta_{AC} \approx 168$ degrees, which is well in excess of our observed values of θ_{A0}. Measurements of θ_{A0} are reported on Fig. 3(b) for the case of varying external phase viscosity η_2 on surfaces 1*b* and on Fig. 3(c) for various topologies at fixed η_2. In these figures, we also report the evolution of the average aspect ratio Γ as a function of σ during sustained growth and find a similar trend. It is found, in particular, that a rough substrate made of a single material, *i.e.*, surfaces 1*c* and 2*c*, displays larger contact angles for low surface fractions σ. The slight increase of θ_{A0} for coated surfaces at low σ, is interpreted based on the larger contact angle on photoresist compared to bare glass. On the one hand, the relative independence of the texture height h on contact angles for the case of immersed droplets suggests the partial capture of oil patches inside the grid bottom basins during the spreading process resulting in a water droplet spreading in a Cassie state. On the other hand, the effective reduced gravity environment during immersed spreading limits significant influence of the height of vertical walls on hydrostatic pressure at the contact line and,

similar to the small influence of horizontal walls – characterized with d – on θ_{A0}, the height h of grid patterns has negligible role on contact angle for droplet in a Wenzel state. In general, data suggest that droplets are in partial Cassie and Wenzel states with complex fluid rearrangements at various time-scales as discussed in following sections. Experimental measurements of local contact angles $\theta_{A0} > \pi/2$ in this work, however, are outside the theoretical range of validity of both Wenzel law, $\cos\theta_{A0} = r\cos\theta_{AC}$ where r is the grid roughness, due to the change of sign of $\cos\theta$ at $\theta = \pi/2$ as well as Cassie law, $\cos\theta_{A0} = \sigma\cos\theta_{AC} + (1-\sigma)\cos\theta_{AB}$, for a droplet resting on coated and bare surfaces with both θ_{AC} and $\theta_{AB} < \pi/2$. While the partial capture of oil patches in grid cavities suggests a modified Cassie law where θ_{AB} is substituted with π similar to the case of air pockets,[45] bottom views typically show that droplet contact lines are primarily pinned on grid lines thereby limiting the use of modified Cassie-Baxter relationships[21] in our case.

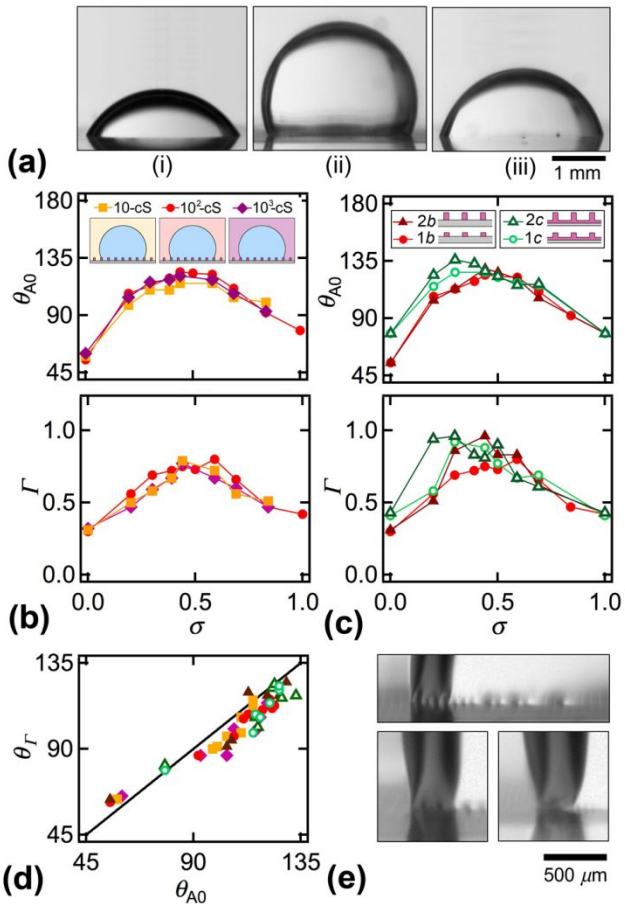

Fig. 3 Evolution of contact angle on patterned surfaces. (a) Micrographs of droplet during relaxation for (i) $\sigma = 0$, (ii) 0.44, and (iii) 1 on surfaces 1*b*. (b) Evolution of maximal contact angle θ_{A0} and aspect ratio Γ on surface *1b* as a function of surface coverage σ for various oil viscosities η_2. (c) Variations of θ_{A0} and Γ versus σ for various h and coatings. (d) Comparison of contact angles based on aspect ratio θ_Γ and direct measurement θ_{A0}. Solid line: $\theta_\Gamma = \theta_{A0}$. (e) Micrographs of dual meniscus for droplet facet and corner.

Overall, contact angles θ_{Γ} based on measurements of Γ and calculated using Eq. 1 slightly underestimate direct measurements of θ_{A0} [Fig. 3(d)]. Indeed, as droplets spread on textured surfaces, planar geometric arrangements of grids introduce anisotropic energy barrier constraints for the contact line, and different contact angles are observed during slow motion along facets and corners of the wetted area. The appearance of a dual meniscus in the profile view on Fig. 3(e) provides evidence of the multiplicity of contact angles along the contact line at a given time. In particular, the measured θ_{A0}, which is typically larger than $\pi/2$, corresponds to the fraction of contact line pinned along a facet, while the apparent contact angle lower than $\pi/2$ corresponds to a droplet corner. Therefore, measurements of θ_{Γ} provide an average measurement of spatially varying contact angles along the wetted area.

These observations suggest that, over the range of parameters investigated, the planar arrangement of textures plays an important role on apparent contact angle due to faceting of the wetted area and corresponding free surface deformation used in the measurement of apparent contact angles. In the following, we examine how surface patterning affect wetting morphologies.

5. Morphology of wetted area

In this section, we study the relationship between the wetted area shape and surface patterning. In particular, our high-resolution image acquisition system allows us to examine contact motion at the grid level as shown in Fig. 4(a) for the case of a large grid size $d = 85$ μm. The quadrille grid of size d provides a reference system for the detailed investigation of the evolution of the radius of curvature r of a droplet corner as a function of the average droplet radius $R = D/2$ where D is the average distance between facets. In figure 4(b), r and R are measured in unit of d and data suggest that $r = \alpha R$ where $\alpha \approx 0.36$ remains constant during forced spreading, which shows that α does not depend on the drop size. The constant α is also significantly lower than unity, which corresponds to the numerical value associated with a disk. Measurements of α are reported on Fig. 4(c) for the same fluid pair on surfaces having various values of d and display similar behavior. Overall, the constant α appears as a smooth function of d on Fig. 4(c).

By analogy with the roundness factor used to characterize the departure of shapes from a circle, the shape of faceted drops can be quantified using the 'squareness' $Sq = 1 - \alpha$, which corresponds to 1 for a square and 0 for a circle. Measurements of Sq are displayed on Fig. 4(d) for series of experiments conducted with various outer fluid viscosity η_2 as a function of surface coverage σ. The overall shape factor Sq is reasonably well fit with a function of the form $Sq = 1 - \sigma$ for $\sigma > 0.3$ as shown in Fig. 4(e), which simply yields $\alpha \sim \sigma$. The relative proportion of faceted drop edges compared to corner wedges qualitatively explains apparent advancing contact angle data, such as the large increase of θ_A at low σ due to grid pinning as displayed in Fig. 3(c).

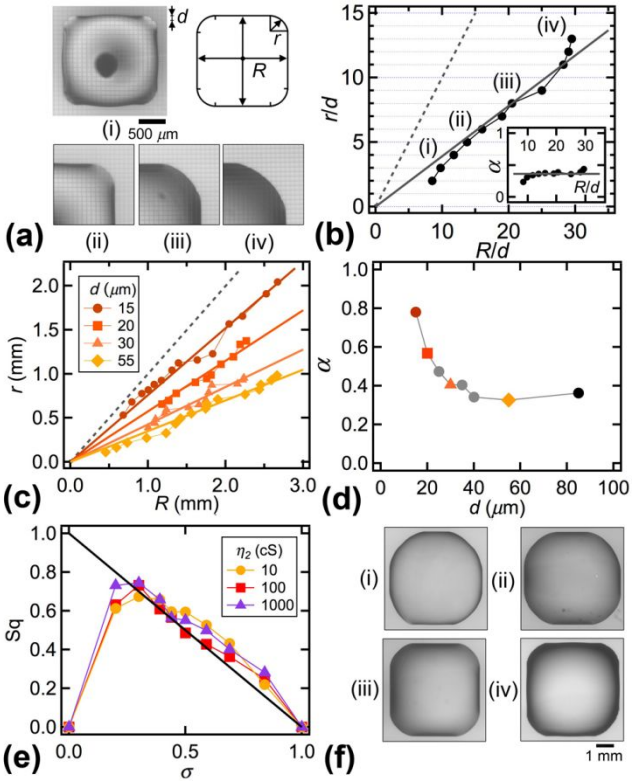

Fig. 4 Faceted growth. (a) Measurements of radius of curvature r of a corner and average droplet radius R. Water in 10-cS oil on surface 1b with d = 85 μm. (b) Evolution of normalized r/d as a function of R/d for the case shown in (a). Solid line: $r/d = \alpha R/d$ with $\alpha = 0.36$. dashed-line: $\alpha = 1$. (c) Variations of r with R for water in 10-cS oil on various substrates. (d) Measurements of α as a function of d for water in 10-cS oil. (e) Droplet squareness Sq versus surface coverage σ for various oil viscosities η_2. Solid line: $Sq = 1 - \sigma$. (f) Micrographs of faceted droplets for water in 10-cS oil: (i) $\sigma = 0.84$, (ii) 0.69, (iii) 0.50, and (iv) 0.30.

While we previously discussed average droplet morphologies, small discrepancies are found in the radius of curvature of each corner for a given droplet as shown on Fig. 4(f). As instances of asymmetrical faceted growth from the injection needle are observed, measurements of α are conducted on the droplet corner the farthest away from the injection point to avoid free surface deformation due to injection apparatus. During the relaxation process, the coefficient α is found to remain constant. As similar trends are observed across all fluid pairs and surfaces, droplet faceting is clearly shown to increase as the grid density σ is lowered.

6. Apparent receding contact angles

We now turn our attention to the deflation process. As the retraction flow rate is set at $Q = 2\mu$L/min at t_3, the withdrawal stage corresponds to a significant decrease of the water drop volume while the wetted area remains stationary. Upon reaching a critical angle at instant t_4, a liquid wedge is seen to slide on a thin deposited film of

water on the patterned surface [Fig. 5(a)]. As the water wedge leaves a thin film on the surface, we label the critical angle at the onset of wedge motion apparent receding contact θ_{R0} since the actual receding contact angle is close to zero degree and cannot be observed using our apparatus. We analyze micrographs generated from profile views to extract the value of the apparent receding contact θ_{R0} [Fig. 5(b)] and find a nearly constant value of $\theta_{R0} \sim 18$ degrees across all textured surfaces and fluid pairs [Fig. 5(c)]. Subsequently, the water wedge is seen to recede after t_4 and an inversion of the free surface curvature is observed. During the apparent dewetting stage most of the initially injected droplet volume is evacuated from the substrate. Measurements of dynamic contact angle enable the quantification of apparent contact angle hysteresis $\Delta\theta_0 = \theta_{A0} - \theta_{R0}$, which displays the shape of a slightly skewed bell curve toward low σ. Quantifying the apparent contact angle hysteresis $\Delta\theta_0$ is of practical use to estimate the overall droplet water volume confined on textured substrates.

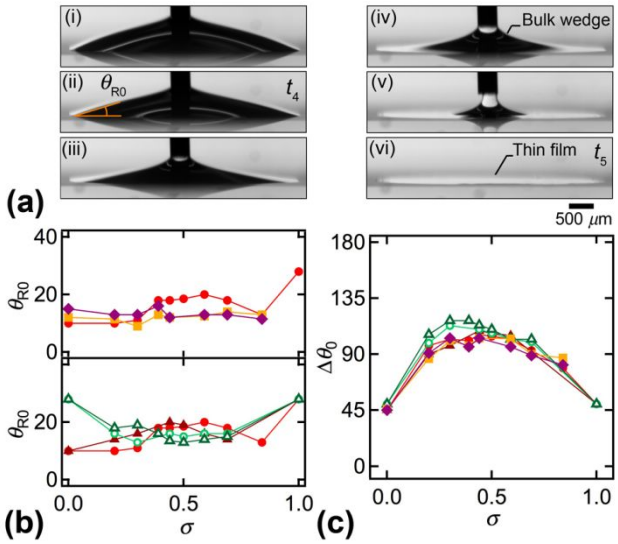

Fig. 5 Droplet withdrawal process. (a) Time-series of profile views of deflation process in 10-cS oil on surface 1*b* with d = 35 μm, Δt = 50 s, frame (ii) corresponds to the instant t_4 when θ_{R0} is measured. (b) Measurements of apparent receding contact angle θ_{R0} as a function of surface coverage σ for various fluids and substrates. (c) Combined apparent contact angle $\Delta\theta$ hysteresis versus σ for all fluids and textures.

7. Water film retraction

As the water wedge recedes, the presence of a thin film is evident from both profile and bottom views [Fig. 6(a)]. In turn, over long period of times, the thin film retracts at an initial average velocity V_R estimated from image analysis [Fig. 6(b)] and the overall mechanism is illustrated on Fig. 6(c). Measurements of V_R as a function σ show the presence of a minimal value V^*_R around d = 30 μm, which corresponds to an intermediate value of σ = 0.5 [Fig. 6(d)]. Experiments conducted while varying the continuous phase viscosity η_2 show a decrease of V^*_R

with outer viscosity according to $V^*_R \sim \eta_2^{-1/3}$ [Fig. 6(d)-inset], which suggests that the external phase capillary number $Ca_2 = \eta_2 V/\gamma_{12}$ alone is not sufficient to predict film dewetting in a viscous ambient phase.

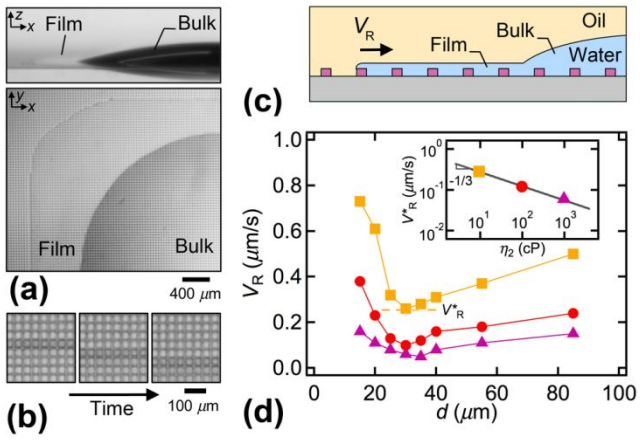

Fig. 6 Dynamics of film retraction. (a) Micrograph of top and profile views for water in 10-cS oil and $d = 40$ μm. (b) Time-series of receding contact line position, $\Delta t = 6$ min. (c) Schematics of film retraction process. (d) Evolution of V_R as a function of d. Inset: evolution of lowest velocity V^*_R vs. η_2. Solid line: $V^*_R = 0.6\ \eta_2^{-0.34}$.

8. Trapped oil droplets

Finally, we discuss the formation and evolution of minute oil droplets trapped in the wells formed by the grid pattern during the spreading process. As the contact line moves across decorated surfaces, some viscous oil patches are found to remain trapped below the main water droplet [Fig. 7(a)]. Over time, square-shaped oil patches coil back to reduce interfacial area and form a variety of small oil droplets. Evidence of the formation of trapped droplets is shown in figure 7(b), where droplets corresponds to darker regions on the substrate due to large interfacial curvature. In particular, the droplet density appears to increase over time in the wake of the contact line since the large viscosity coefficient of the oil phase compared to that of the water $\eta_2 \gg \eta_1$ introduce relatively 'slow' oil droplet coiling compared to 'fast' water drop dynamics.

While small viscous oil droplets seem to appear randomly during sustained growth of water droplets, oil droplet density is usually large below the injection point where the contact line velocity was sufficiently large during the initial spreading stage to capture oil patches in grid wells. The shape of densely populated oil droplet areas is also correlated with the water droplet spreading direction as seen in Fig. 7(b)(iv), where droplet clusters stretch normal to the contact line direction.

The presence of trapped droplets is particularly apparent during the film retraction process where a thin film of water can remain anchored to an oil droplet cluster as represented on Fig. 7(c). An example of such cluster is shown on Fig. 7(d) with the help of micrographs taken at various magnifications, including the large-scale view used to record dynamics as well as photographs taken through an inverted microscope where the container was

carefully placed at the end of the experiment. The microscope views show complex film rearrangement over coated droplets as well as individual droplet arrangement in each cavity.

In the course of these experiments, the long-term evolution of trapped oil droplets consists of a mix of coated droplet and coalescing droplets depending on local flow history as shown on Fig. 7(e). While the presence of coated droplets is seen in the microscopic views, coalescing droplets are also observed during film retraction over densely populated regions over long periods of time as shown in Fig. 7(f).

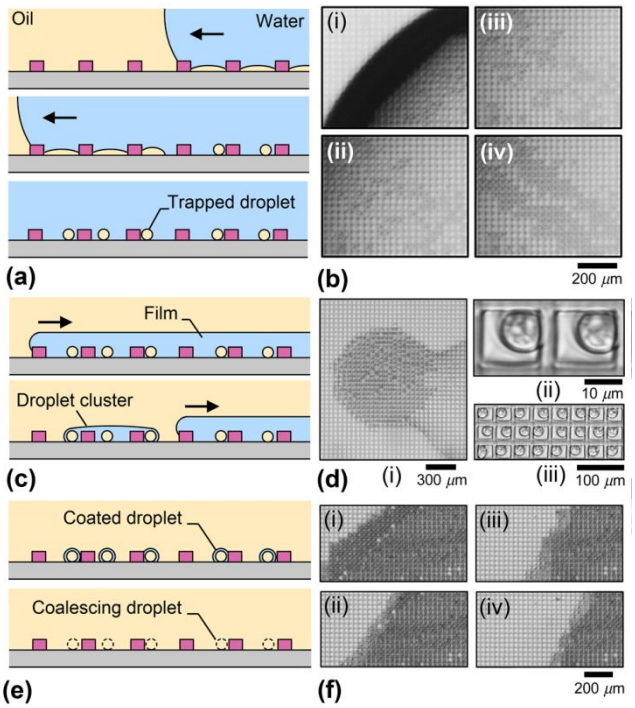

Fig. 7 Phenomenology of trapped oil droplets. (a) Schematics of formation process with oil patch capture and droplet coiling. (b) Time-series of micrographs with increase in oil droplet density over time from (i) to (iv) with Δt = 10 min, surface 2*c* with d = 35 μm (c) Sketch of cluster formation during film retraction. (d) Micrographs of droplet cluster on surface 2b with d = 40 μm at various magnifications with complex droplet coating. (e) Illustration of coated and coalescing droplets. (f) Time-series of dewetting process over high-density of coalescing droplets, surface 2*b* with d = 35 μm, Δt = 1 hour.

The appearance of oil droplets in grid cavities is reminiscent of the trapping of gas bubbles during the spreading of water on rough hydrophobic surfaces in air for $\theta_A > \pi/2$. The partial wetting conditions of grid patterns in our experiment, however, suggest the existence of a critical cavity aspect ratio Λ_C for the onset of oil droplet capture. Indeed, while considering a contact line at the top edge of a grid pattern clarifies the presence of large apparent contact angles, conversely when a contact line advances toward the bottom edge of a grid pattern of height h, a simple geometrical construction with a straight free surface indicates that a cavity of length s is

expected to trap an oil patch if $s/h \leq \Lambda_C$, where the critical aspect ratio reads $\Lambda_C = \tan \theta_A$ [Fig. 8(a)]. Here, as $s = d - (w_x+w_y)/2$, the evolution of $\Lambda = s/h$ with the grid coverage σ is displayed on Fig. 8(b) for the two different grid heights, h_1 and h_2, used in the experiment and the line $\Lambda_C = \tan 78° \approx 4.7$ demarks anticipated regions of trapped oil droplets from those with clean surfaces. Incidentally, although the evolution of Λ_C with θ_A is evident, it is noteworthy to consider the divergence of Λ_C near $\pi/2$. Hence, our approach reveals an intriguing regime of partial wetting with relatively large angles θ_A where wide dead-end pores with large Λ can readily capture oil patches. By contrast, for low contact angles, such as $\theta_A < \pi/4$, only deep cavities with $\Lambda < 1$ can potentially capture oil droplets.

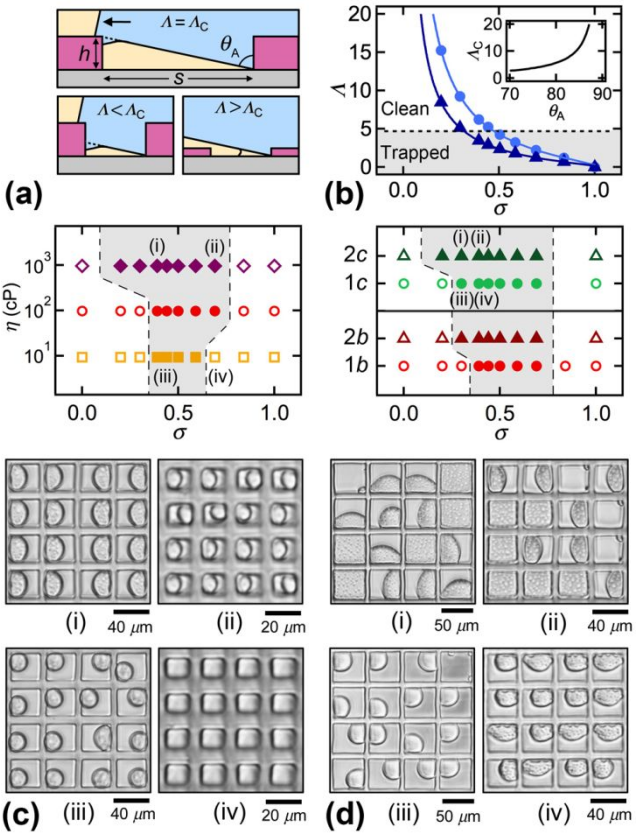

Fig. 8 Trapped droplets. (a) Illustration of the role of cavity aspect ratio $\Lambda = s/h$ on droplet trapping with $\theta_A = 78°$. (b) evolution of Λ with σ for h_1 (●) and h_2 (▲), dashed-line: $\Lambda_C = 4.7$. Inset: evolution of Λ_C with advancing contact angle θ_A, solid line: $\Lambda_C = \tan \theta_A$. (c and d) Regime maps of trapped droplets (closed symbols) and clean surfaces (open symbols). (c) Top: Observed occurrence of trapped droplets for experiments conducted at various oil viscosity η_2 and surface coverage σ. Bottom: High-magnification micrographs of surface near injection area. (d) Top: Map of trapped droplet based on surface property and coverage σ. Bottom: High-magnification micrographs of coated surface with coated oil patches and droplets.

Overall, our experiments confirm this finding as can be seen on the various regime maps of trapped oil droplets in Figs. 8(c) and 8(d). For the experimental series conducted while varying the external phase viscosity η_2, we

find that the domain of droplet presence as a function of σ increases with η_2, which is consistent with the fact that the oil patch capture increases with oil viscosity [Fig. 8(a)]. For experiments interrogating the influence of coating and grid height h, we find more trapped droplets occurrence as h increases. In this case, data suggest a value of Λ_C corresponding to contact angles in slight excess of θ_A, which is consistent with the increase of θ_A with velocity according to standard dynamic contact angle analysis.

Overall, while the typical size of trapped oil droplets scales with d, a great variety of morphologies are observed for a given substrate depending on location. In addition, the position of a droplet in a cell is dependent upon the flow history and droplets sometimes appear located near the well's wall closest to flow direction as shown in Fig. 8(a)(iii) for a large grid. For large grid heights, oil patches and droplets appear pigmented with smaller droplets suggesting potential Ostwald ripening phenomena between water and silicone oils over long period of times.

9. Conclusions

In this work, we examine the wetting dynamics of liquid-liquid systems on a variety of microtextured surfaces at multiple scales using a sessile drop method. We first show that, when immersed in a liquid phase, the droplet aspect ratio Γ decreases monotonically during the droplet inflation-deflation process with a plateau during the sustained growth stage. The characteristic Γ is compared with direct measurements of advancing contact angles on composite surfaces. The presence of a square grid pattern significantly influences the shape of the droplets, which display faceted growth with apparent contact angles $\theta > \pi/2$ larger than contact angles $\theta < \pi/2$ found on individual smooth components due to significant pinning on grid edges. The morphology of the wetted area is analyzed based on the ratio of the radius of curvature of droplet corner to the mean droplet radius to calculate the squareness coefficient that is found to linearly depends on the grid surface coverage. In the retraction regime, we find a nearly uniform apparent receding contact angle associated with the initial retraction of a water wedge from the surface leaving a thin film at the surface. Information about advancing and receding contact angle enables the calculation of the apparent contact angle hysteresis $\Delta\theta$, which primarily depends on σ and is relatively independent of h and fluid viscosities in the quasi-static regime at very small capillary numbers.

Natural droplet relaxation dynamics and film retraction velocity are found in the range of 100 nm/s. Given the large viscosity of the external phase, experiments show the presence of trapped oil droplets under the main water drop at the surface. We develop a criterion for the onset of oil trapping in dead-end pores of various aspect ratios and examine the morphology and arrangement of residual oil drops using multiple magnifications to reveal coated droplet and coalescing droplets. Finally, we discuss the role of surface characteristics and fluid property on the occurrence of trapped oil droplets.

Overall, this work shows rich wetting dynamics with a roughness-induced transition from partial wetting to partial non-wetting in a previously poorly explored region of parameter space. Future work could investigate the

role of droplet viscosity and flow rate in the presence of surfactant during natural and forced wetting and dewetting of microtextured surfaces to fully characterize the water-oil wetting dynamics on complex liquid-infused and immersed surfaces.

Acknowledgements

This material is based upon work supported by the National Science Foundation under Grant No. CBET-1605809.

Conflicts of interest

The authors declare no competing financial interest.

References

1 W. L. Olbricht, *Annu. Rev. Fluid Mech.,* 1996, **28**, 187.

2 S. F. Shariatpanahi, S. Strand, and T. Austad, *Energy & Fuels,* 2010, **24**, 5997.

3 E. Crestel, A. Kvasničková, E. Santanach-Carreras, J. Bibette, and N. Bremond, *Phys. Rev. Fluids,* 2020, **5**, 104003.

4 G. J. Dunderdale, C. Urata, T. Sato, M. W. England, and A. Hozumi, *ACS Applied Materials & Interfaces,* 2015, **7**, 18915.

5 D. Ge, L. Yang, C. Wang, E. Lee, Y. Zhang, and S. Yang, *Chem. Comm.,* 2015, **51**, 6149.

6 Y. Lu, S. Sathasivam, J. Song, C. R. Crick, C. J. Carmalt, and I. P. Parkin, *Science,* 2015, **347**, 1132.

7 J. R. Landel and D. I. Wilson, *Annu. Rev. Fluid Mech.,* 2021, **53**, https://doi.org/10.1146/annurev.

8 D. Brutin, Droplet wetting and evaporation: from pure to complex fluids. Academic Press: 2015.

9 K. Koch, B. Bhushan, and W. Barthlott, *Soft Matter,* 2008, **4**, 1943.

10 C.-C. Chang, C.-J. Wu, S. Y-.J., and H.-K. Tsao, 2015, **11**, 7308.

11 D. Quéré, *Ann. Rev. Mater Res.,* 2008, **38**, 71.

12 H. Bazyar, P. Lv, J. A. Wood, S. Porada, D. Lohse, and R. G. H. Lammertink, *Soft Matter,* 2018, **14**, 1780.

13 F. Schellenberger, J. Xie, N. Encinas, A. Hardy, M. Klapper, P. Papadopoulos, H.-J. Butt, and D. Vollmer, *Soft Matter,* 2015, **11**, 7617.

14 M. Muschi, B. Brudieu, J. Teisseire, and A. Sauret, *Soft Matter,* 2018, **14**, 1100.

15 B. Zhao, C. W. MacMinn, and R. Juanes, *Proc. Natl. Acad. Sci.,* 2016, **113**, 10251.

16 B. M. Jose, D. Nandyala, T. Cubaud, and C. E. Colosqui, *Sci. Rep.,* 2018, **8**, 14159.

17 L. Keiser, A. Keiser, M. L'Estimé, J. Bico, and E. Reyssat, *Phys. Rev. Lett.,* 2019, **122**, 074501.

18 B. M. Jose and T. Cubaud, *Phys. Rev. Fluids,* 2017, **2**, 111601(R).

19 R. N. Wenzel, *Industrial & Engineering Chemistry,* 1936, **28**, 988.

20 A. Cassie and S. Baxter, *Trans. Faraday Soc.,* 1944, **40**, 546.

21 W. Choi, A. Tuteja, J. M. Mabry, R. E. Cohen, and G. H. McKinley, *J. Colloid Int. Sci.,* 2009, **339**, 208.

22 A. Giacomello, S. Meloni, M. Chinappi, and C. M. Casciola, *Langmuir,* 2012, **28**, 10764.

23 D. Murakami, H. Jinnai, and A. Takahara, *Langmuir,* 2014, **30**, 2061.

24 M. E. Kavousanakis, C. E. Colosqui, I. G. Kevrekidis, and A. G. Papathanasiou, *Soft Matter,* 2012, **8**, 7928.

25 D. M. Spori, T. Drobek, S. Zürcher, and N. D. Spencer, *Langmuir,* 2010, **26**, 9465.

26 C. Priest, T. W. J. Albrecht, R. Sedev, and J. Ralston, *Langmuir,* 2009, **25**, 5655.

27 N. Anantharaju, M. V. Panchagnula, S. Vedantam, S. Neti, and S. Tatic-Lucic, *Langmuir,* 2007, **23**, 11673.

28 T. Cubaud and M. Fermigier, *J. Colloid Interface Sci.,* 2004, **269**, 171.

29 Y. C. Jung and B. Bhushan, *Langmuir,* 2009, **25**, 14165.

30 S. Mitra, N. S. K. Gunda, and S. K. Mitra, *RSC Advances,* 2017, **7**, 9064.

31 T. Cubaud and M. Fermigier, *Europhys. Lett.,* 2001, **55**, 239.

32 L. Courbin, E. Denieul, E. Dressaire, M. Roper, A. Ajdari, and H. A. Stone, *Nature Materials,* 2007, **6**, 661.

33 H. Kusumaatmaja and J. M. Yeomans, *Langmuir,* 2007, **23**, 6019.

34 R. J. Vrancken, M. L. Blow, H. Kusumaatmaja, K. Hermans, A. M. Prenen, C. W. M. Bastiaansen, D. J. Broer, and J. M. Yeomans, *Soft Matter,* 2013, **9**, 674.

35 S. Yada, S. Bagheri, J. Hansson, M. Do-Quang, F. Lundell, W. van der Wijngaart, and G. Amberg, *Soft Matter,* 2019, **15**, 9528.

36 T. D. Blake and K. J. Ruschak, *Nature,* 1979, **282**, 489.

37 J. H. Snoeijer, G. Delon, M. Fermigier, and B. Andreotti, *Phys. Rev. Lett.,* 2006, **96**, 174504.

38 G. G. Wells, E. Ruiz-Gutiérrez, Le Lirzin, Y., A. Nourry, B. V. Orme, M. Pradas, and R. Ledesma-Aguilar, *Nature Comm.,* 2018, **9**, 1380.

39 C. Semprebon, G. McHale, and H. Kusumaatmaja, *Soft Matter,* 2017, **13**, 101.

40 J. H. Guan, G. G. Wells, B. Xu, and G. McHale, *Langmuir,* 2015, **31**, 11781.

41 J. D. Smith, R. Dhiman, S. Anand, E. Reza-Garduno, R. E. Cohen, G. H. McKinley, and K. K. Varanasi, *Soft Matter,* 2013, **9**, 1772.

42 X. Hu, Z. Wang, D. J. Hwang, and T. Cubaud, *Langmuir,* 2020, **36**, 9269.

43 H. Jeon, H. Hidai, D. J. Hwang, and C. P. Grigoropoulos, *J. Biomed. Mater Res.,* 2010, **93A**, 56.

44 H. Jeon, H. Hidai, D. J. Hwang, K. E. Healy, and C. P. Grigoropoulos, *Biomaterials,* 2010, **31**, 4286.

45 Y. C. Jung and B. Bhushan, *Langmuir,* 2009, **25**, 14165.

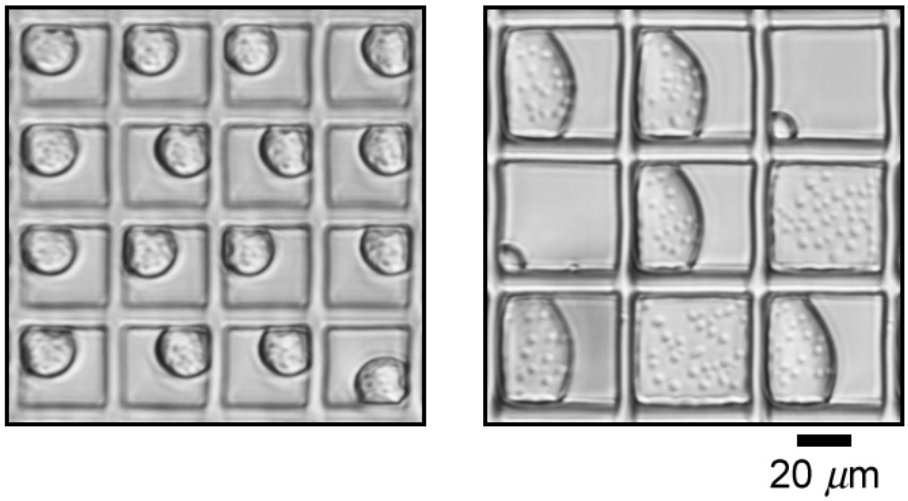

62x31mm (300 x 300 DPI)